

Flat silicon gradient index lens with deep reactive-ion-etched 3-layer anti-reflection structure for millimeter and submillimeter wavelengths

Fabien Defrance, *Senior Member, IEEE*, Cecile Jung-Kubiak, *Senior member, IEEE*, John Gill, Sofia Rahiminejad, *Member, IEEE*, Theodore Macioce, Jack Sayers, Goutam Chattopadhyay, *Fellow, IEEE*, and Sunil R. Golwala

Abstract—We present the design, fabrication, and characterization of a 100 mm diameter, flat, gradient-index (GRIN) lens fabricated with high-resistivity silicon, combined with a three-layer anti-reflection (AR) structure optimized for 160–355 GHz. Multi-depth, deep reactive-ion etching (DRIE) enables patterning of silicon wafers with sub-wavelength structures (posts or holes) to locally change the effective refractive index and thus create anti-reflection layers and a radial index gradient. The structures are non-resonant and, for sufficiently long wavelengths, achromatic. Hexagonal holes varying in size with distance from the optical axis create a parabolic index profile decreasing from 3.15 at the center of the lens to 1.87 at the edge. The AR structure consists of square holes and cross-shaped posts. We have fabricated a lens consisting of a stack of five 525 μm thick GRIN wafers and one AR wafer on each face. We have characterized the lens over the frequency range 220–330 GHz, obtaining behavior consistent with Gaussian optics down to -14 dB and transmittance between 75% and 100%.

©2024. All rights reserved.

I. INTRODUCTION

Broadband observations at millimeter and submillimeter wavelengths are critical for many topics in astronomy and cosmology, including CMB polarization measurements of cosmological parameters, Sunyaev-Zel’dovich effect studies of hot cosmological plasmas, observations of dust thermal emission and atomic fine-structure lines from the dusty interstellar medium both in our galaxy and at extragalactic and cosmological distances, and molecular spectroscopy of planetary atmospheres. Silicon’s high refractive index ($n = 3.42$), achromaticity, lack of birefringence, high thermal conductivity, mechanical strength, and low loss make it an ideal optical material at these wavelengths. However, its index also presents a challenge for anti-reflection (AR) treatment.

The standard AR treatment for a material with refractive index n_{bulk} is a quarter-wavelength layer of dielectric material with index $n_{AR} = \sqrt{n_{bulk}}$. Multiple layers with appropriate indices yield broader bandwidths. To keep ghost images below

an acceptable level, a typical reflectance requirement is $<1\%$ (two sides combined; *for power, not field*)

Few materials, however, are appropriate matches for silicon. Plastics such as parylene and cirlex provide narrow bandwidths, have non-negligible loss, and do not have the correct index to achieve $<1\%$ reflectance [1], [2]. Epoxy-based coatings achieve wider bandwidths but do not meet the reflectance requirement and have appreciable loss: 2- and 3-layer coatings achieve $<10\%$ reflectance over, respectively, 2.7:1 and 3.2:1 spectral bands, with 1% and 10% loss [3]. Plasma spray coatings [4] and artificial dielectric metamaterials [5], [6] perform similarly.

An alternative is to reduce silicon’s effective refractive index using sub-wavelength features. Such structures inherently address loss and thermal contraction and can be non-birefringent at normal incidence.

The dicing saw approach [7], yielding multi-layer AR microstructures of posts, has been very successful: it was/is deployed in ACTPol [8], Advanced ACTPol [9], and ToTEC [10] and is planned for Simons Observatory [11], [12], SPT-3G+ [13], CCATp [14], [15], and CMB-S4 [16]. The most advanced versions deployed/planned are 3-layer structures providing $<0.5\%$ reflectance over 2.3:1 bandwidth [17]. A 5-layer, 5:1 bandwidth version was designed and tested, but it was non-optimal in that the thinnest saw blade used was 20 μm rather than the thinnest available 12 μm , and a mean reflectance $>1\%$ was expected and observed [17]. Due to a practical limit on the ratio of cut depth (total AR thickness) to blade width of 50:1 [17], a 4-layer, 3.6:1 bandwidth structure is the widest bandwidth deemed achievable with this approach [17]. Scaling the deepest cut’s width from 20 μm for the 100-400 GHz design in [17] to 12 μm would yield a 165–600 GHz treatment.

Another group has cut pyramids with a beveled blade, sometimes in combination with a dicing saw to cut square pillars [18]–[20]. The best results achieved are $<5\%$ reflectance over 2.9:1 bandwidth (87–252 GHz) [18].

Laser machining has also been used on silicon. The earliest efforts used sharp cones [21] and concentric circular grooves [22]. The most successful approach has used pyramidal structures. [18] obtained approximately 3% reflectance over 1.8:1 and 2.4:1 bandwidths (170–300 and 202–490 GHz), respectively. [23] found a factor 1.45 increase in gain when such a structure was used instead of parylene-C for silicon lenslets at 500 GHz. [24] explored cylindrical and conical

Corresponding author: fabien.m.defrance@jpl.nasa.gov

F. Defrance, C. Jung-Kubiak, J. Gill, S. Rahiminejad, and G. Chattopadhyay are with the Jet Propulsion Laboratory, California Institute of Technology, Pasadena, CA, 91109 USA.

J. Sayers and S. R. Golwala, are with the California Institute of Technology, Pasadena, CA, 91125 USA.

T. Macioce was with the California Institute of Technology, Pasadena, CA, 91125 USA and is now with Hughes Research Laboratories, 3011 Malibu Canyon Road, Malibu, CA, 90265 USA.

structures appropriate for silicon lenslets and found that $<5\%$ reflectance may be achievable. Laser machining is thus not yet as performant as the dicing saw approach, but it may be the only non-laminate option for lenslets with radius of curvature much smaller than that available with dicing saws.

An alternative is deep reactive ion etching (DRIE), a mature technique capable of aspect ratios up to 30:1. Multi-depth DRIE [25] can etch layers of differing effective refractive index n_{eff} in a single wafer. Stacking of multiple wafers yields the high layer-count structures needed for wide bandwidths. DRIE permits posts and holes of various shapes (e.g. square, circular, cross, hexagonal), providing design flexibility needed for very wide bandwidths. DRIE has been used for 1-layer THz structures on flat surfaces [26]–[31]. A 2-layer THz post structure has been fabricated for wider bandwidth, but test results were not presented [26]. In prior work, we provided the first demonstration of a 2-layer DRIE structure, yielding $<1\%$ reflectance over 1.6:1 bandwidth (190–310 GHz) [32]. [33] later used a similar design at THz frequencies, with multi-layer silicon-on-insulator (SOI) wafers for etch stops, but did not report reflectance measurements. Another group extended this approach to a 3-layer structure, but with 2.4% mean reflectance 200–450 GHz [34], [35].

By designing the etch pattern to yield radial variation of n_{eff} , a flat-faced GRIN optic can be produced. However, unlike AR structures, a GRIN lens design may only use holes so it can be physically continuous and thus edge-mountable. While DRIE depth and aspect ratio limitations constrain individual wafers to be no more than 0.5–2 mm thick, wafer stacking provides a solution: the focal length scales inversely with the total thickness of the stack, and independent AR wafers can be stacked with the GRIN optic. We present here the design, fabrication process, and test results for a flat silicon GRIN lens with 3-layer AR structures on each side, building on preliminary results provided in [36].

II. DESIGN

A. GRIN lens: theoretical design

A Wood lens [37] is a flat optic with focusing provided by a power-law dependence of the refractive index on radius [38]:

$$n_{\lambda}(r) = N_{0,\lambda} + N_{1,\lambda}r^2 + N_{2,\lambda}r^4 + \dots \quad (1)$$

where $n_{\lambda}(r)$ is the refractive index of the lens for a wavelength λ and at a distance r from the optical axis, and $N_{i,\lambda}$ are real coefficients that may depend on wavelength. In practice, only a finite number of coefficients is possible. The simplest and most common Wood lens uses only the two first $N_{i,\lambda}$ coefficients [39]–[41], which corresponds to a parabolic index profile. We have chosen this profile for this work for the sake of simplicity. Because our design aims to provide a lens that is intrinsically achromatic over the 160–355 GHz frequency range of interest, we take the $N_{i,\lambda}$ to be wavelength-independent,

$$n(r) = N_0 + N_1r^2, \quad (2)$$

with N_0 the index of the lens on the optical axis ($N_0 = n(0)$). For a focusing GRIN lens (see Figure 1), the maximum index is located at $r = 0$ and the minimum index is at $r = R$, where

R is the radius of the edge of the lens’s focusing region (the physical radius must be larger than R to provide an unetched mounting surface). We may thus write $n(0) = n_{\text{max}}$ and $n(R) = n_{\text{min}}$, and Equation 2 becomes

$$n(r) = n_{\text{max}} - (n_{\text{max}} - n_{\text{min}}) \frac{r^2}{R^2}. \quad (3)$$

We show in Appendix A that a lens with the above parabolic index gradient and thickness t yields, in air, an achromatic focal length

$$f = n_{\text{air}} \frac{R^2}{2t(n_{\text{max}} - n_{\text{min}})}. \quad (4)$$

While the choice of a parabolic index profile has the benefit of simplicity and no spherical aberration at low focusing power ($R \ll f$), such aberration may become significant for higher-power optics (see Appendix A). Aberrations in Wood lenses have been studied by Cadwell [38] and Nguyen et al. [42]. A higher-order Wood lens can reduce spherical aberration but suffers coma [38]. Curved Wood lenses [42] and multi-element Wood lens systems [38] can simultaneously correct for spherical aberration, coma, astigmatism, and field curvature. Other $n(r)$ functions can be considered, such as the generalized Mikaelian lens [43]–[45] (hyperbolic secant dependence) and the generalized Luneburg lens ($n(r) = (\beta/f) [1 + f^2 - (r/R)^2]^{1/2}$) [46]–[48]. While these designs are widely used to focus light in the GRIN medium itself (e.g., light propagation in optical fibers) without aberrations [46], [48], there is little information in the literature about their use with two GRIN-air interfaces (i.e., as a stand-alone optical element).

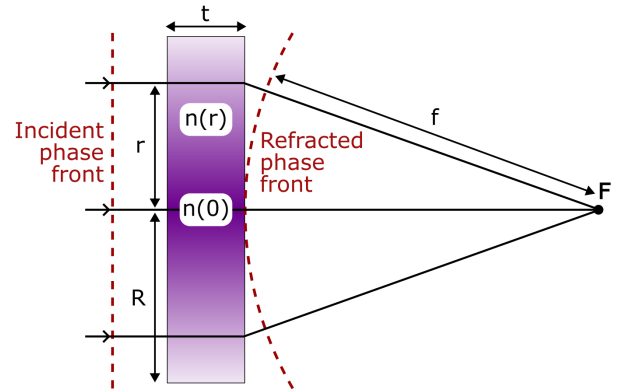


Fig. 1. Schematic showing the operation and parameters of a GRIN lens. The variation of the speed of light across the lens yields a radial dependence of the optical path length, which causes an incident flat phase front to acquire the radius of curvature of a converging wave that comes to a focus at F . The optic thus focuses with focal length f . The choice of a parabolic index profile results in negligible spherical aberration in the paraxial/low-power approximation ($R \ll f$), but spherical aberration becomes significant when the approximation is violated (see discussion in text).

In [36], we performed a physical optics simulation of a lens of the above design, using the Ray-Launching Geometrical Optics (RL-GO) solver of the commercial software Feko¹. We took $n_{\text{min}} = 1.87$, $n_{\text{max}} = 3.25$, $R = 40$ mm, and

¹<https://altair.com/feko>

$t = 7.7$ mm to obtain a focal length $f = 75$ mm. In practice, it is challenging to vary the index continuously, so we approximated the parabolic dependence with fixed indices, linearly spaced between n_{min} and n_{max} over 30 concentric annuli with radial thickness decreasing as $1/r$. The lens presented in this paper is based on this preliminary design, but the maximum index was reduced to $n_{max} = 3.15$ and the thickness decreased to $t = 2.625$ mm for reasons described in sections II-B and III.

B. GRIN lens: mask design

The demonstrated GRIN lens comprises a stack of silicon wafers, each patterned with sub-wavelength holes etched through the wafers using deep reactive-ion etching (DRIE) in order to locally change the effective refractive index of the wafer, as described by [32]. The holes reside on a grid, hexagonal in this case, with sub-wavelength unit cell size. Variation of the hole size with lens radius yields the desired index variation, while, for simplicity, the unit cell size does not vary. Figure 2 shows the hexagonal unit cell, with Λ the unit cell size, and $r_c = \Lambda/2$ and r_h the center-to-flat distance for the cell and the hole, respectively.

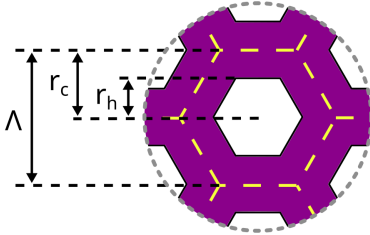


Fig. 2. Schematic of a single GRIN lens cell (cross-section view). The white regions are holes, the purple area is silicon, and the yellow dashed lines represent the unit cell boundary.

As DeFrance et al. [32] showed, the dependence of effective refractive index n_{eff} on unit cell parameters can be represented in a universal manner by relating the index to the silicon fill factor, the ratio of the volume of silicon to the unit cell volume, f_{Si} :

$$f_{Si} = \frac{V_c - V_h}{V_c}, \quad (5)$$

where V_h and V_c are the hole and unit cell volumes. If the holes have a constant cross-section (vertical walls), Equation 5 reduces to:

$$f_{Si} = \frac{A_c - A_h}{A_c}, \quad (6)$$

where A_h and A_c are the hole and unit cell cross-sectional areas. For hexagonal holes and cells as shown in Figure 2, we may rewrite Equation 6 as

$$f_{Si} = \frac{r_c^2 - r_h^2}{r_c^2}. \quad (7)$$

We used simulations with Ansys Electronic Desktop software to determine that a unit cell size $\Lambda = 75$ μm is sufficiently smaller than the wavelength at the highest frequency of interest for our planned application, 425 GHz, to render n_{eff} achromatic. We then simulated a range of values of r_h at this

fixed value of Λ to find the mapping between f_{Si} and n_{eff} , as previously reported in [36]. Finally, we used this mapping to calculate the variation of r_h with r needed to obtain the desired parabolic (or, in the future, any other) index profile.

Practical considerations drive the choice of the parameters n_{min} , n_{max} , and R used to define the index profile in Equation 3. We use 100 mm diameter wafers but we set $R = 40$ mm to provide an unpatterned border for mounting. The thinnest achievable wall size, $r_c - r_h^{max}$ where r_h^{max} is the dimension of the largest holes, determines n_{min} and is limited by mechanical robustness. We chose $r_c - r_h^{max} = 15$ μm based on past experience, yielding $n_{min} = 1.87$. The maximum refractive index, n_{max} , is limited by the maximum DRIE aspect ratio, the ratio of etch depth to minimum transverse dimension for holes. Since our fabrication approach incorporates etching from both sides, the etch depth is half the wafer thickness. We use 525 μm wafers because they are an industry standard and also because the wafer thickness is not critical,² resulting in an etch depth of 262.5 μm . Using the DRIE machine's nominal maximum etch aspect ratio of 30:1 would have resulted in holes with $r_h = 4.4$ μm and $n_{max} = 3.39$. There was little advantage, however, to such a stringent demand on the machine's performance: reducing the aspect ratio to 20:1 or 15:1 would only reduce n_{max} to 3.35 and 3.29, respectively. We chose a slightly more conservative approach, with the smallest holes having dimension $r_h^{min} = 9.3$ μm , etch aspect ratio 14:1, and $n_{max} = 3.25$. In the end, the reduction in n_{max} from 3.39 to 3.25, combined with $n_{min} = 1.87$, only increases the focal length by 10%.

Preliminary fabrication efforts for the above design revealed a strong dependence of etch rate on hole dimension, yielding a strong variation of etch rate across the lens. Waiting for completion of the slower-etching features (smallest holes) resulted in over-etch of the faster-etching features (largest holes), yielding incorrect hole dimensions and profiles. To obtain a uniform etch rate, we modified the mask to leave an unetched sacrificial pillar at the center of each hole so that the transverse etch dimension, and thus the etch aspect ratio, could be approximately independent of r_h and location on the wafer, as Figure 3 illustrates. Implementation of the pillars over the entire etched area requires annulus width $w \leq r_h^{min}$: if $w > r_h^{min}$, holes with $r_h^{min} < r_h < w$ have no pillars. The other consideration is aspect ratio, which motivates larger w . The largest value for w consistent with pillars over the entire etched area, $w = r_h^{min} = 9.3$ μm , however, yields aspect ratio 28:1, approaching the maximum aspect ratio allowed, 30:1. The annulus aspect ratio becomes so large because the previous highest aspect ratio was set by $2r_h^{min}$, not r_h^{min} . To balance these two considerations, we choose $w = r_h^{min}$ but decrease n_{max} to 3.15 so r_h^{min} increases to 11.8 μm , yielding a highest aspect ratio of 22:1. The further small reduction in n_{max} yields a focal length 8% and 19% larger than for $n_{max} = 3.25$ and $n_{max} = 3.39$. Reliable production of the

²One might surmise that thicker wafers would reduce the number of wafers and thus etch steps required. The etch aspect ratio limitation, however, implies thicker wafers would result in smaller n_{max} and thus the overall thickness t of the optic would have to increase, partially canceling the benefit of thicker wafers. The converse argument holds for thinner wafers.

pillars fails at very small pillar size, so we eliminate the pillars when their radius is $\leq 0.2 \mu\text{m}$. This choice retains pillars at radii from the center of the lens greater than 3.5 mm, corresponding to 99.2% of the etched area.

Figure 5 shows the final dependence of hole radius, pillar radius and annulus width on radius. Figure 4 shows the final GRIN wafer design.

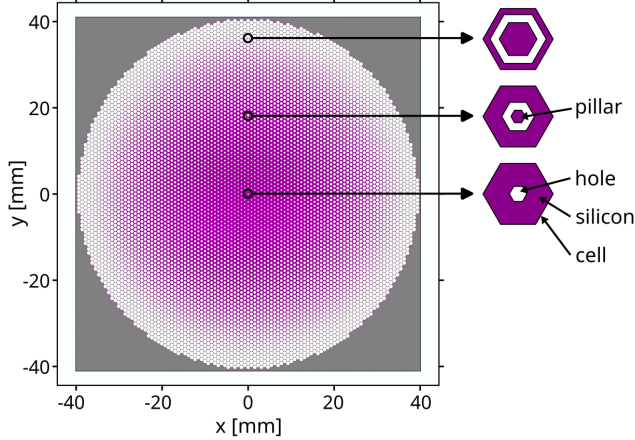


Fig. 3. Schematic of the 80 mm diameter etched area of the GRIN lens. The schematic is not to scale in order to make the features legible. Purple is silicon while white is material that has been removed by DRIE. The insets on the right show the evolution of hole and pillar geometry with radius.

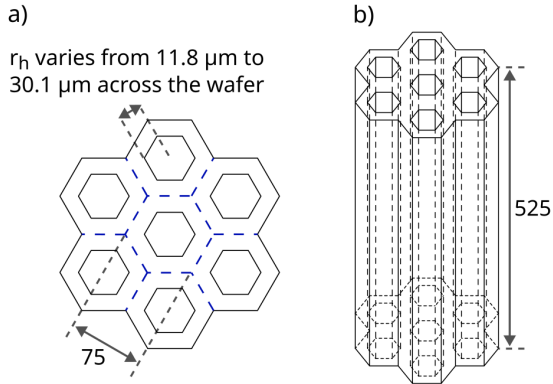


Fig. 4. a) Top view of a GRIN lens wafer, with the blue dashed lines delimiting the unit cell with $\Lambda = 2r_c = 75 \mu\text{m}$. The design (not DRIE mask) hole transverse dimension r_h varies from $11.8 \mu\text{m}$ at the center ($n_{max} = 3.15$) to $30.1 \mu\text{m}$ at the edge ($n_{min} = 1.87$). b) Isometric view of GRIN lens wafer design. The total height of $525 \mu\text{m}$ corresponds to a single wafer thickness. Several identical wafers are stacked together to make the GRIN lens.

After implementing the pillars, further fabrication tests revealed the need for corrections to the mask design to account for DRIE non-idealities. The etched dimensions were consistently larger than the mask dimensions by a few μm (over-etching), and the tests showed a 0.5–1.5 degree taper of the holes, narrowing with depth. We calculated a depth-averaged fill factor and revised the hole dimensions accordingly, and we also corrected the mask for over-etching, resulting in transverse mask etch dimensions 6–7 μm smaller than the desired hole diameters (with radius dependence). Figure 5 shows the final choices for transverse dimension correction

and pillar dimension (including that correction) as a function of radius.

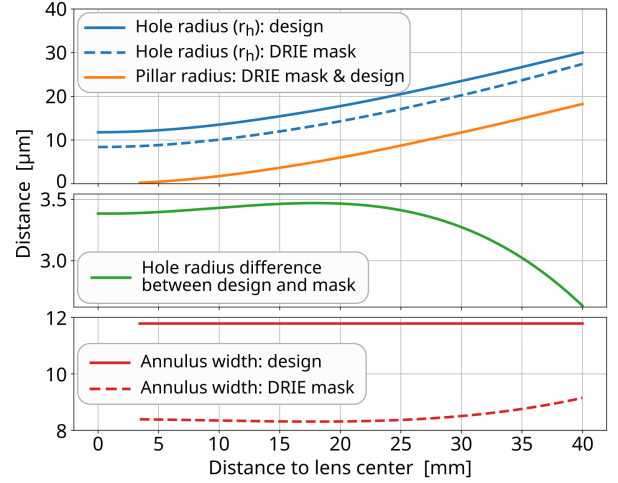


Fig. 5. Top: Design and mask value for hole radius (r_h) and pillar radius as a function of distance from center of the GRIN lens. For pillars, the design and DRIE mask dimensions are the same. Pillars are only added to holes when their radius is larger than $0.2 \mu\text{m}$. Middle: Difference between the design and mask hole radii (r_h), which is the transverse dimension correction explained in the text. The correction was determined empirically using test etches. Bottom: Transverse design and mask width of hexagonal annulus as a function of distance from center of the GRIN lens. The pillar radius is designed to create an etched annulus with constant width across the lens (plain red line). The DRIE mask annulus width is the difference of the mask value of r_h and the pillar radius.

C. Anti-reflective structures: theoretical design

Any powered optic requires anti-reflection (AR) treatment: the same refractive index mismatch that enables focusing also causes a reflection. For the effective refractive index range implemented here, $n_{eff} \in [1.87-3.15]$, the reflectance at any one interface due to index mismatch with air would be 9–27% and radially dependent. In general, the ideal AR treatment for a GRIN optic would vary both the index and the AR thickness with radius. For example, a quarter-wavelength treatment optimized for free-space wavelength λ_0 would have $n_{AR}(r) = \sqrt{n_{eff}(r)/n_{air}}$ and $t_{AR}(r) = \lambda_0/4n_{AR}(r)$. Our approach, however, can only provide planar AR layers.

We approximate the ideal AR treatment by a radius-independent AR treatment, the design of which should be chosen based on the desired spectral band and a beam-power-weighted average of $n_{eff}(r)$ over radius:

$$\langle n_{GRIN} \rangle = \frac{\int 2\pi r dr I_{beam}(r) n_{eff}(r)}{\int 2\pi r dr I_{beam}(r)}. \quad (8)$$

For testing purposes here, we illuminate the GRIN lens with a Gaussian beam, whose intensity distribution is:

$$I_{beam}(r) = e^{-2r^2/\omega^2}, \quad (9)$$

with ω the beam radius (see Section IV for details on Gaussian optics and beam radius) at the lens and r the distance from the optical axis (center of the lens). For Gaussian optics, it is

usually recommended for optical elements to have diameter no smaller than 4ω ; under these conditions, only 0.03% of the power is intercepted, and diffraction due to this truncation is negligible. We have designed our test setup (Section IV) to meet this criterion by illuminating the GRIN lens with $\omega = 18.5$ mm at 275 GHz. We calculate $\langle n_{GRIN} \rangle = 2.99$ assuming this illumination.

To demonstrate progress toward the eventual goal described in Section I of wide-bandwidth GRIN optics, we chose a wide-bandwidth 3-layer AR treatment, tuned for 160–355 GHz. It was feasible to accommodate this specific band with a structure whose overall thickness matches the easily available 525 μm wafer thickness. However, we designed and fabricated the 3-layer AR wafer before we reduced the GRIN n_{max} from 3.25 to 3.15 as described in Section II-B, and thus it was designed for $\langle n_{GRIN} \rangle = 3.08$. We discuss the expected impact of this slightly non-optimal design below.

We optimized the AR design in a manner similar to our prior design work ([32], [36], [49]) using quarter-wavelength Chebyshev matching transformer theory ([50]; see Chapter 5.7 of [51] for a pedagogical exposition). The Chebyshev approach has broader bandwidth than other stepped approaches such as the binomial transformer and requires fewer layers than stepped tapers like the Klopfenstein taper [51]. We followed an existing implementation method ([52]; [53] Chapter 6.8) with a requirement of sub-1% ripples to obtain the layer indices and thicknesses in Table I. We calculate the power-weighted reflectance for the AR-treated GRIN optic in a manner similar to the calculation of the power-weighted refractive index:

$$\langle |S_{11}(f)|^2 \rangle = \frac{\int 2\pi r dr I_{beam}(r) |S_{11}(r, f)|^2}{\int 2\pi r dr I_{beam}(r)}, \quad (10)$$

where $S_{11}(r, f)$ is calculated as a function of r assuming the parabolic $n_{eff}(r)$ profile for the GRIN lens (Section II-B) and the 3-layer AR structure design (Table I) using standard methods ([52]; [53] Chapter 6.8).³ Figure 6 displays the results, both for the original GRIN design with $n_{max} = 3.25$ and the revised design with $n_{max} = 3.15$, showing that the expected impact of the less optimal AR design is too small to warrant re-fabrication of the 3-layer AR for this demonstration.

TABLE I
OPTIMAL QUARTER-WAVELENGTH CHEBYSHEV TRANSFORMER THEORY REFRACTIVE INDICES AND THICKNESSES FOR 3-LAYER AR, ASSUMING FIXED 525 μm TOTAL AR WAFER THICKNESS AND $\langle n_{GRIN} \rangle = 3.08$.

	Refractive index	Thickness [μm]
Layer 1 (L1)	1.21	243
Layer 2 (L2)	1.75	167
Layer 3 (L3)	2.54	115

³Note that the reflectance calculation assumes effective refractive indices; it is not a full EM simulation of the patterned structure.

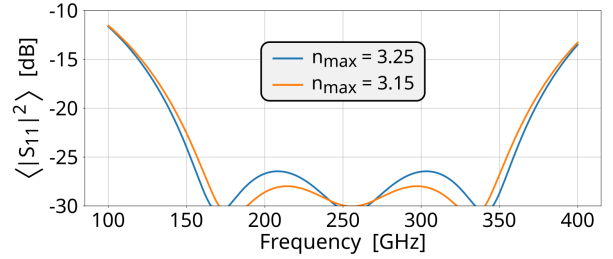


Fig. 6. Calculated beam-weighted reflectance at the interface between air and the GRIN lens, including the 3-layer AR structure, for the original and revised GRIN designs with $n_{max} = 3.25$ and $n_{max} = 3.15$.³

D. Anti-reflective structures: mask design

Given the desired effective indices for the AR layers in Table I, the next step is to choose shapes and dimensions of sub-wavelength structures to realize them. It has been shown, both analytically [54] and by simulation [32], that structures with N -fold rotation symmetry, $N \geq 2$, are non-birefringent, rendering square, circular, hexagonal, or cross shapes, and both posts and holes, all acceptable. Defrance et al. [32], [36] calculated the effective index of these structures as a function of f_{Si} (defined in Section II-B). Where possible (L2 and L3), we use holes because they are more mechanically robust and provide a continuous structure. For $n_{eff} \lesssim 1.6$ (L1), we choose posts because holes would have walls too thin to be reliably fabricated with our DRIE machine.

The least challenging DRIE process involves etching L1/L2 from one side and L3 from the other. We choose square holes for L2 and L3.⁴ One approach to ensuring consistency of L1 and L2 — the L1 unetched silicon must not overlap the L2 etched region — is to use cross posts for L1 with features no larger than the L2 wall thickness. For the goal bandwidth, 160–355 GHz, a cell size of 100 μm is sufficient to ensure achromaticity. Reducing the cell size in the future to match the GRIN cell size, 75 μm , will ensure the AR structure functions well up to 425 GHz.

We find the dimensions of the sub-wavelength structures layer-by-layer using Ansys Electronic Desktop (previously HFSS) by varying the dimensions to obtain a match to the S -parameters of a homogeneous slab with the desired effective index (Table I). We show the optimized 3-layer AR structure design in Figure 7.

E. High resistivity silicon loss tangent

Our GRIN and AR wafers are made of high-resistivity (>10 k Ω -cm) silicon. Knowing the absorption loss of these wafers is useful for setting an upper limit on the maximum achievable power transmittance of the lens at room temperature (at cryogenic temperatures, high-resistivity silicon absorption is much lower). As shown in Pozar [51] (Chapter 1.3), the complex permittivity ϵ of a medium can be expressed as:

$$\epsilon = \epsilon' - j\epsilon'' = \epsilon'(1 - j \tan \delta), \quad (11)$$

⁴Circular holes have non-uniform wall thickness, demanding the thinnest walls for a given f_{Si} , and thus are disfavored. Hexagonal holes may be a better choice than square holes because of the larger angle at the corners.

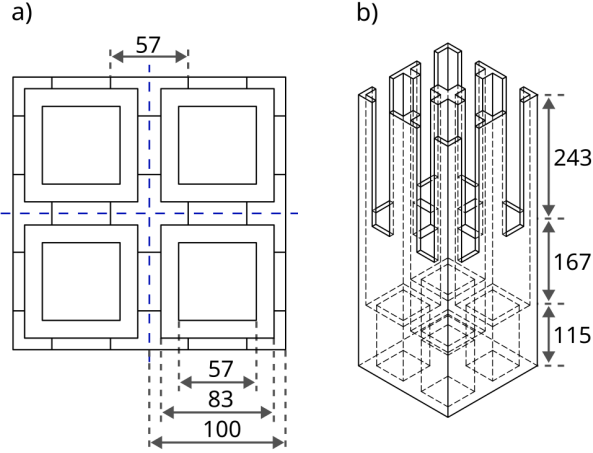


Fig. 7. a) Top view of the 3-layer AR structures. The top cross posts are complementary with the middle-layer square holes, so both can be etched from the same side. b) Isometric view of the AR structures. All dimensions are in μm .

with $\tan \delta$ the loss tangent of the medium (and $j = \sqrt{-1}$). Two different sources of loss contribute [51]: pure dielectric loss due to the damping of oscillating dipole moments ($\tan \delta_d$) and conductivity loss ($\tan \delta_c$). Incorporating the [55], [56] expression for the latter (and using $\varepsilon'_r = \varepsilon'/\varepsilon_0$), we have

$$\tan \delta = \tan \delta_d + (2\pi\nu\rho\varepsilon'_r\varepsilon_0)^{-1}. \quad (12)$$

Table II summarizes microwave [57] and terahertz [58] measurements of $\tan \delta_f$ and ε'_r for high-resistivity, float-zone silicon at room temperature, including the impact of various treatments. There is no measurable dependence on frequency between 1 and 330 GHz, with values for $\tan \delta_d$ and ε'_r in the ranges 11.65–11.72 and $1\text{--}4 \times 10^{-5}$, respectively. We use $\varepsilon'_r = 11.7$ and $\tan \delta_d = 4 \times 10^{-5}$ below. For conduction loss, $\rho > 10 \text{ k}\Omega\text{-cm}$ implies $\tan \delta_c < 9.6 \times 10^{-5}$ at 160 GHz and $< 4.3 \times 10^{-5}$ at 355 GHz and therefore $\tan \delta < 14 \times 10^{-5}$ at 160 GHz and $< 8 \times 10^{-5}$ at 355 GHz. The power absorbance in an optic of thickness d is

$$A = \left(\frac{2\pi\nu\sqrt{\varepsilon'_r}\tan\delta}{c} \right) d \quad (13)$$

$$A < (1.6 \text{ m}^{-1})(3.675 \text{ mm}) = 0.006 \text{ at } 160 \text{ GHz} \quad (14)$$

$$A < (0.9 \text{ m}^{-1})(3.675 \text{ mm}) = 0.007 \text{ at } 355 \text{ GHz} \quad (15)$$

These absorbance values set approximate upper limits on power transmittance T . The upper limits are not precise because the absorbance values are upper limits; T may be higher if A is lower.

III. FABRICATION

The 100 mm diameter, 525 μm thick, high-resistivity ($>10 \text{ k}\Omega \text{ cm}$), float-zone silicon wafers used for both GRIN and AR structures satisfy the following additional specifications: double-sided optically polished; bow/warp $<30 \mu\text{m}$, thickness variation $<5 \mu\text{m}$, <10 particles above $0.3 \mu\text{m}$ in size per face, $\langle 100 \rangle$ crystal orientation, and light n-type phosphorus doping.

TABLE II
DIELECTRIC LOSS TANGENT AND REAL RELATIVE PERMITTIVITY MEASUREMENTS AT ROOM TEMPERATURE FOR VARIOUS FLOAT-ZONE SILICON SAMPLES.
HP: HIGH PURITY; HR: HIGH RESISTIVITY; DLR: GOLD-DOPED LOW-RESISTIVITY SILICON; EHR: ELECTRON-IRRADIATED HR-Si; PHR: PROTON-IRRADIATED HR-Si.
RESISTIVITY IS ENHANCED BY GOLD DOPING [59] AND IRRADIATION.

	HP [58]	HR [58]	DLR [58]	EHR [58]	PHR [57]
ν [GHz]			30–330		1–15
$\tan \delta_d \times 10^5$	1	3–4	1	2	1.2
ε'_r		11.67–11.72			11.65
ρ [$\text{k}\Omega\text{-cm}$]	48	17	51	42	52

For this demonstration, we used 5 GRIN wafers and 2 AR wafers, each 525 μm thick. The GRIN thickness is a compromise between fabrication time — five GRIN wafers, plus two wafers for dimensional confirmation, required approximately five months for fabrication process development and production — and testing capabilities — a lens too thin would have a focal length too large for our test setup.

A. GRIN lens

The GRIN wafer fabrication process involves the patterning of a radius-dependent hole pattern (see Figure 3) all the way through the wafer, which we accomplish by doing DRIE through a SiO_2 mask successively on both sides of the wafer. We begin by thermally growing 3.8 μm of oxide on both sides of the wafer in a furnace in a wet environment. We etch the hole patterns into the SiO_2 on both sides of the wafer, using a 6 μm AZ4330 photoresist (PR) mask, exposed using a Heidelberg MLA150 Maskless Aligner, and fluorine-based inductively coupled plasma reactive ion etching (ICP RIE). The patterned SiO_2 serves as the mask for DRIE, which we perform to a depth of half the wafer thickness.⁵ We then protect the now-complete first side with a layer of spray-on PR to prevent over-etching of the existing holes and repeat the DRIE and cleaning steps on the second side, joining the holes from the two sides. The process of cleaning the patterned wafers with PR remover and solvents also washes away the unetched pillars (Section II-B), and we remove residual SiO_2 with a 49% hydrofluoric acid (HF) solution.

Figure 8 shows optical images of the GRIN wafer holes, including cross sections from a sacrificial wafer. A slight tapering with depth is evident, which we measure and can then account for by revising the mask so the average hole diameter matches the design value.

⁵We use a 150 mm Plasma-Therm Versaline. Mounting our 100 mm wafers to 150 mm carrier wafers using thermal paste is necessary. Because of the large DRIE etching load, good thermal contact of the wafer to the wafer chuck (which provides cooling) is critical. Following DRIE, we clean the wafers with solvents and oxygen plasma.

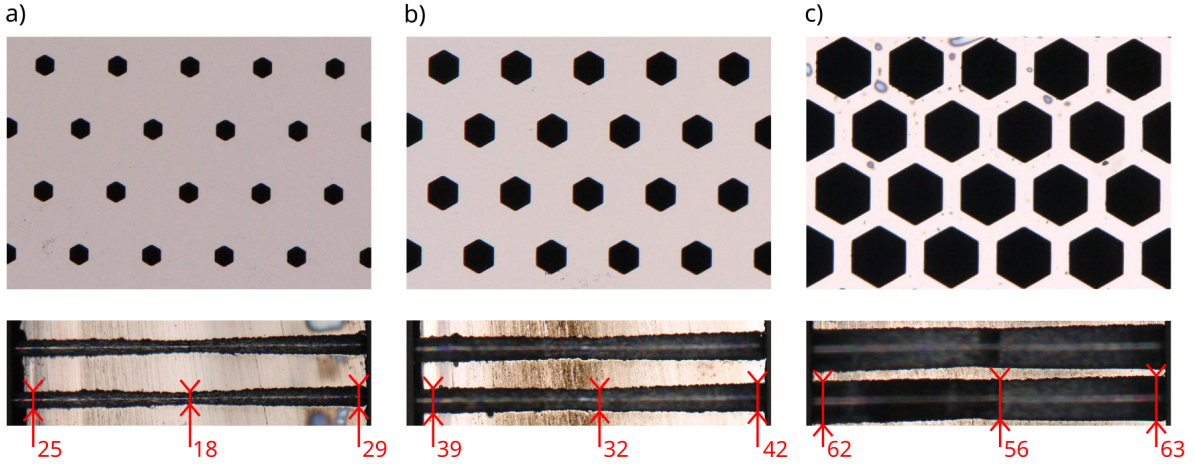


Fig. 8. Top view and cross-sectional optical microscope images ($\times 400$ magnification) of a $525\ \mu\text{m}$ GRIN lens wafer at radii of a) $0\ \text{mm}$, b) $20\ \text{mm}$, and c) $40\ \text{mm}$. The hole diameters (in μm) at various depths are indicated in red. Recall that the wafers are etched to a depth of half the wafer thickness from both sides. The tapering of the holes with depth is accounted for so that the fill factor averaged over depth matches the design value.

We then align and stack the wafers, making use of $500\ \mu\text{m}$ long and $1\ \text{mm}$ diameter silicon dowel pins placed in $300\ \mu\text{m}$ deep pockets etched into the outer $10\ \text{mm}$ of each wafer at the same time as the GRIN holes. The pockets on the two sides of a wafer are clocked relative to one another so each pin only aligns two wafers. The alignment precision is better than $10\ \mu\text{m}$, rendering artifacts due to misalignment unobservable in measurements.

B. AR structures

We fabricate the $525\ \mu\text{m}$ AR wafers by etching L3 from one side and L1/L2 from the other.⁶ As for the GRIN wafers, we first grow $2.6\ \mu\text{m}$ of SiO_2 to act as a mask during DRIE. We etch L3 in the same manner as the holes for the GRIN wafers, first patterning the oxide using a $5\ \mu\text{m}$ AZ5218 PR photolithography and then using the SiO_2 as the mask for DRIE, performed to a depth of $115\ \mu\text{m}$. We again use spray-on PR to protect the etched L3 side. For the L1/L2 etch, we use a variant of the multi-step DRIE process we developed in [25]. We first pattern the SiO_2 using PR photolithography with the L1 cross post pattern as we did for L3. We then spin on, expose, and develop a thick PR layer ($10\ \mu\text{m}$ AZ9260) *on top of the already patterned SiO_2 mask* with the L2 hole pattern. Two DRIE steps follow. The first uses the thick PR mask to etch L2 to a depth of $167\ \mu\text{m}$. We clean off any residual PR with PR remover (requiring dismounting from and then remounting on the carrier wafer) and then perform a second DRIE step using the pre-etched SiO_2 mask to etch the L1 cross post pattern to a depth of $243\ \mu\text{m}$. During L1 etching, the previously patterned L2 holes also etch $243\ \mu\text{m}$ deeper, yielding the two-depth L1/L2 structure.

Figure 9 shows scanning electron microscope (SEM) images of the 3-layer AR structure. The dimensions measured via SEM are consistently within 5% of design values.

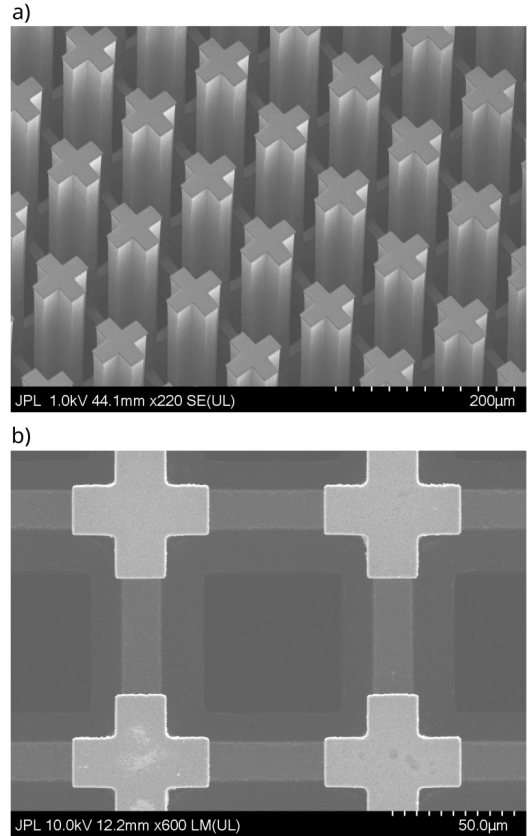


Fig. 9. Scanning electron microscope images of a 3-layer AR structure. a) Isometric view showing the L1 cross-post and L2 square-hole layers. b) Top view showing all three layers.

Finally, we add an AR wafer on each side of our 5 GRIN wafers assembly, using the same silicon dowel pins and etched pockets scheme mentioned in Section III-A.

⁶See Section II-D for layer definitions.

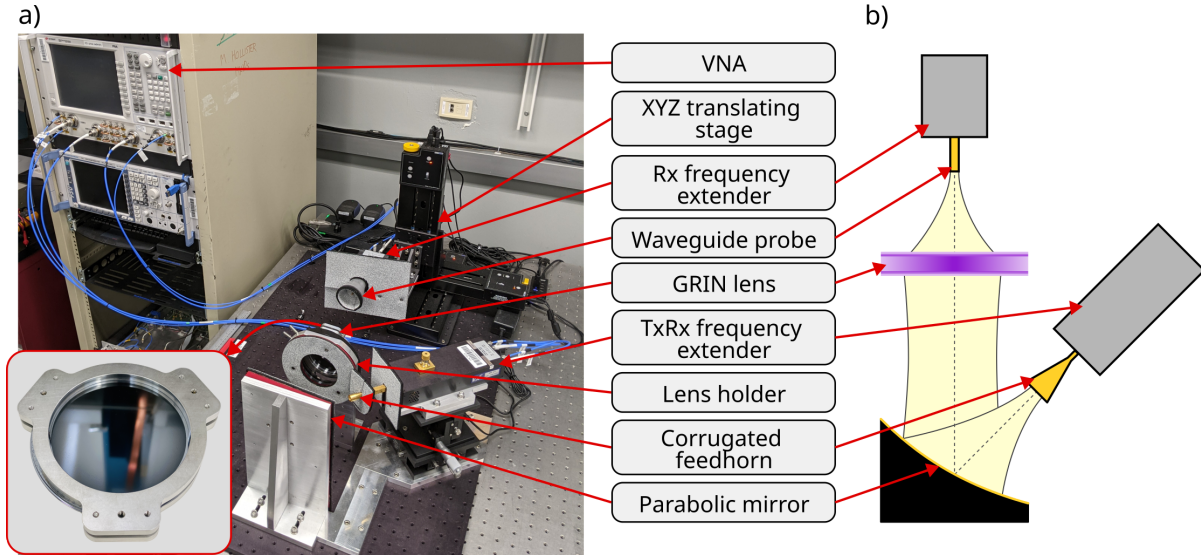


Fig. 10. Beam scan measurement setup. a) Picture of the test bench used to characterize the GRIN lens, with a picture of lens mounted in its holder in the lower left insert. b) Schematic of the test setup, only keeping the optical elements for clarity.

IV. OPTICAL TESTING

The GRIN lens, composed of a stack of 5 GRIN wafers and 2 AR wafers (one on each side of the stack), was characterized at room temperature, under normal illumination, and over the frequency range 220–330 GHz.

A. Measurement Setup and Gaussian Optics Expectations

Figure 10 shows the setup. We used a vector network analyzer (VNA)⁷ with frequency extenders⁸ as the source and receiver. We couple power out from the source using a corrugated feedhorn⁹, which provides a nearly Gaussian beam¹⁰. Table III gives the feedhorn’s design parameters.

TABLE III
CORRUGATED FEEDHORN DESIGN PARAMETERS

Frequency [GHz]	220	275	330
Far-field divergence angle [°]	19.4	16.2	14.5
Gain [dB]	24.2	25.7	26.7
Beam waist radius, ω_0 [mm]	2.54	2.44	2.28
Distance between beam waist and feedhorn aperture [mm]	8.95	11.78	14.30

⁷Keysight N5222A

⁸Virginia Diodes WR3.4VNATxRxM-5M

⁹Radiometer Physics GmbH custom-designed for 220-330 GHz, WM-864 (WR-3.4) waveguide

¹⁰In Gaussian optics, the beam waist is the location on the optical axis where the beam radius is the smallest, the radius of curvature is infinite, and intensity on the optical axis is maximal. The beam radius at the beam waist is called beam waist radius and written ω_0 . The beam radius, ω , (at any location, not just at the beam waist) is the radius at which the electric field magnitude is reduced by $1/e$ relative to its peak value on-axis. The far-field divergence angle is the asymptotic growth angle of the beam radius in the far-field limit. For a feedhorn, the beam waist is located inside the horn at a frequency-dependent distance from the aperture.

We place the horn so its output Gaussian beam waist at 275 GHz is located at the focus of an off-axis parabolic mirror¹¹, which has an effective focal length of 119 mm, is 101.6 mm in diameter, and folds the beam by 45°. Though the feedhorn beam waist location moves along the optical axis by 4.35 mm between 220 GHz and 330 GHz (Table III), the effect on the optical propagation and the beam profile at the final beam waist is negligible. The beam exiting the parabolic mirror illuminates the 80 mm diameter patterned region of the GRIN lens. The VNA extender receiver is coupled to a WR-3 waveguide probe mounted on a three-dimensional translation stage¹² (the *beam-mapper*) to construct 3D maps (*beam maps*) of the *electric field magnitude and phase* of the beam focused by the lens. For these maps, we define the Z axis to be along the optical axis and X and Y to be the horizontal and vertical directions transverse to the optical axis.

If geometrical optics were applicable here, the above setup would present a collimated ray bundle to the lens, which would then focus the bundle to a point at its focal length, all achromatically. In Gaussian optics, the beam radius evolution is inherently chromatic, but it is possible to choose the lens location so it creates the Gaussian equivalent: an achromatic image of the source, which is how the GRIN lens would in general be used in an application (e.g., an achromatic image of the sky in an astronomical instrument). For any optic in our setup, we define d_{in} and d_{out} as the distances between the lens and the beam waists before and after the optic (input and output sides). Gaussian optics relates these distances, and the beam radii at the two waists, to each other (e.g., [60]):

$$d_{out} = f + \frac{d_{in} - f}{(d_{in}/f - 1)^2 + z_R^2/f^2} \quad (16)$$

¹¹Edmund Optics 35-628

¹²3× ThorLabs LTS150, computer-controlled

$$\omega_{0,out} = \frac{\omega_{0,in}}{\sqrt{(d_{in}/f - 1)^2 + z_R^2/f^2}}, \quad (17)$$

where $z_R = \pi\omega_{0,in}^2/\lambda$ is the ‘‘Rayleigh range’’, f is the focal length of the lens, and $\omega_{0,in}$ the beam waist radius before the lens.¹³ We obtain achromatic behavior for the location of the beam waist¹⁴ when we set $d_{in} = f$, yielding:

$$d_{out} = f \quad (18)$$

$$\omega_{0,out} = \omega_{0,in} \frac{f}{z_R}. \quad (19)$$

For our setup, we thus obtain achromatic behavior if we set $d_{mir,in} = f_{mir}$ and $d_{GRIN,in} = f_{GRIN}$, yielding $d_{mir,out} = f_{mir}$ and $d_{GRIN,out} = f_{GRIN}$, and if we place the parabolic mirror and GRIN lens a distance $d_{mir,out} + d_{GRIN,in} = f_{mir} + f_{GRIN}$ apart. This configuration is outlined in Figure 11, with $F_{mir,in}$, $F_{mir,out}$, $F_{GRIN,in}$, and $F_{GRIN,out}$ being the positions of the input and output beam waists for the parabolic mirror and GRIN lens.

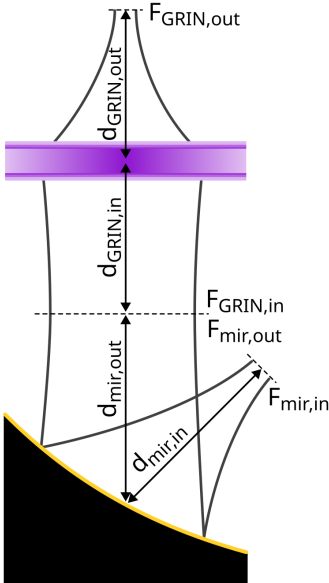


Fig. 11. Schematic of the optical configuration of the GRIN lens test setup, not to scale. As discussed in the text, to obtain achromatic locations of all the beam waists, we choose $d_{mir,in} = f_{mir}$ and $d_{GRIN,in} = f_{GRIN}$ so that $d_{mir,out} = f_{mir}$ and $d_{GRIN,out} = f_{GRIN}$ are obtained. $F_{mir,in}$, $F_{mir,out}$, $F_{GRIN,in}$, and $F_{GRIN,out}$ indicate the locations of these beam waists. We place the beam waist of the corrugated feedhorn source at $F_{mir,in}$ and scan the beam near $F_{GRIN,out}$.

B. Characterization of the Measurement Setup

In our optical setup, $f_{mir} = 119$ mm and the theoretical value of f_{GRIN} is 238 mm. After placing the lens a distance $f_{mir} + f_{GRIN} = 357$ mm from the mirror, we measured $d_{GRIN,out} \approx 220$ mm. Using this measurement as a new value

¹³Note that [60] uses ‘‘confocal distance’’ for what most authors term the ‘‘Rayleigh range’’ and that other authors define the confocal distance as twice the Rayleigh range. To avoid confusion, we use the unambiguous term ‘‘Rayleigh range’’ here.

¹⁴The beam waist radius is unavoidably chromatic due to the throughput theorem, $A\Omega = \lambda^2$.

for f_{GRIN} , we repositioned the GRIN lens 339 mm after the parabolic mirror. We still measured $d_{GRIN,out} \approx 220$ mm, indicating that we had achieved our intended configuration to within our measurement precision and that results would only be weakly dependent on the GRIN lens position.

To check the Gaussian optics calculation before testing the GRIN lens, we placed the beam-mapper at the intended location of the GRIN lens, $d_{mir,out} + d_{GRIN,in} = f_{mir} + f_{GRIN} = 339$ mm from the parabolic mirror. Figure 12 shows the resulting beam map. The beam is highly Gaussian down to $|S_{21}| = 0.1$ with beam radii of 18.8 mm and 18.3 mm along the X and Y axes, respectively. We calculate the expected beam radius using the above Gaussian optics formalism. The beam emitted by the corrugated feedhorn at 275 GHz has a design beam waist radius of $\omega_{0,horn} = 2.44$ mm, located at $F_{mir,in}$, which the parabolic mirror reimages to a beam waist at $F_{mir,out}$ with radius given by Equation 19, $\omega_{0,mir} = 17.0$ mm. We may then calculate the beam radius at the intended location of the GRIN lens by using the standard Gaussian optics propagation equation (e.g., [60]):

$$\omega = \omega_0 \sqrt{1 + \left(\frac{\lambda z}{\pi\omega_0^2}\right)^2}. \quad (20)$$

For $\omega_0 = \omega_{0,mir}$, $z = d_{GRIN,in}$, and $\lambda = 1.09$ mm (275 GHz), we obtain $\omega = 17.6$ mm. The difference from the measured beam radius of 18.6 mm (averaging the X and Y radii) is 6%. Equations 19 and 20 imply this discrepancy could be explained by a 6% error in feedhorn’s beam waist $\omega_{0,horn}$, a 7% error in the distances along the optical axis, or a combination of both. For our measurement, the only impact is that we should use the measured, rather than theoretical, beam radius at the GRIN lens for further propagation calculations.

C. Characterization of the GRIN Lens with AR Treatment

1) *Beam Waist Location:* We placed the GRIN lens at its intended location and the beam-mapper at the expected beam waist location at $F_{GRIN,out}$, a distance $d_{GRIN,out} = 220$ mm after the lens. To locate the optical axis after the lens, we conducted successive one-dimensional X and Y scans with increasingly finer steps to identify the point of maximum intensity, achieving an accuracy better than 0.2 mm. To then locate the Z position of the beam waist, we again did one-dimensional scans in each of the X and Y coordinates, with the other coordinate set to the optical axis located in the previous step, at 51 Z values spaced by 2 mm and centered on the expected beam waist location and at 56 frequencies spaced by 2 GHz from $\nu = 220$ to 330 GHz. For each value of Z and ν , we fitted Gaussians to the X and Y scans and averaged them to estimate the beam radius. For each frequency, we identified the beam waist as the location of the minimum beam radius. We plot the location and radius of the beam waist as a function of frequency ν in Figure 13a). We find no trend in the location with frequency, confirming that we have both correctly chosen an achromatic optical configuration and that the lens is, as expected, achromatic over this frequency range.

The mean value of $d_{GRIN,out}$ is 218 mm, consistent with that noted earlier. The discrepancy between the designed and

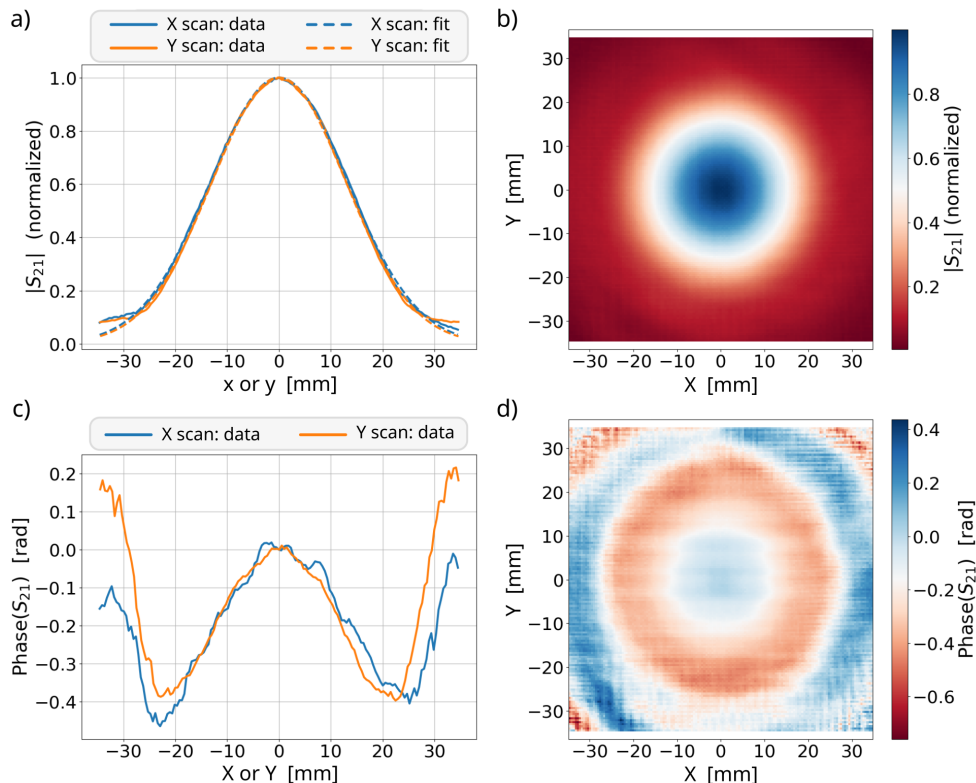


Fig. 12. Beam map at the intended location of the GRIN lens at 275 GHz. a), b) Peak-normalized electric field magnitude $|S_{21}|$; c), d) electric field phase relative to its value on the optical axis. a), c) show 1D scans along X (at $Y = 0$) and Y (at $X = 0$).

measured focal length, 238 mm vs. 218 mm, can be explained by the etch dimension uncertainties. From Equation 4, we calculate that the index range necessary to obtain $f_{GRIN} = 218$ mm is $n_{max} - n_{min} = 1.4$, while the designed range is $3.15 - 1.87 = 1.28$. An increase in n_{max} , a decrease in n_{min} , or a combination of both could be the cause. The extreme cases require that r_h^{min} be $3 \mu\text{m}$ smaller or r_h^{max} be $1 \mu\text{m}$ larger than designed. While the etching precision for the hole radius is about $0.5 \mu\text{m}$, the variation of hole radius with depth results in an accuracy of $1\text{--}1.5 \mu\text{m}$ over the wafer thickness. Therefore, the focal length discrepancy is plausibly and most easily explained by a discrepancy in r_h^{max} . As with other corrections discussed in Section II-B, we can make an empirical correction for this hypothesized effect, which will also serve to unambiguously test this hypothesis.

Knowing the beam waist radius at the input of the GRIN lens, the focal length of the lens, and applying Equation 19, we can calculate the theoretical value of the beam waist radius at the output of the GRIN lens as a function of frequency. Figure 13b) shows that the measured beam waist radius is in good agreement with theoretical expectations for a focal length of 218 mm.

The peak-to-peak range and standard deviation of the fluctuations in $d_{GRIN,out}$ are ± 10 mm and ± 3.6 mm, respectively. These variations seem rather large, but, to estimate their significance, it is useful to compare the fractional difference in the values of the beam radius measured at $d_{GRIN,out}(f)$ and $\langle d_{GRIN,out}(f) \rangle$. Figure 13c) shows that 75% of the points have fractional radius variations $\leq 0.5\%$,

demonstrating that the beam waist position is consistent with $\langle d_{GRIN,out}(f) \rangle = 218$ mm to high precision over the full 220–330 GHz frequency range. The remaining 25% of the points show excursions of up to almost 4%, but they occur near specific frequencies, not randomly over the frequency range. This structure suggests these excursions are caused by standing waves within the setup or the lens. Standing waves within the setup do not impact the lens performance, while standing waves within the lens can be caused by gaps between the stacked wafers. We discuss such potential gaps in more detail in Section IV-C3.

2) *Beam Profile at Beam Waist*: To further characterize the performance of the GRIN lens, we made a full beam map at the beam waist at 275 GHz, shown in Figure 14. We found that measurements over the range 220–330 GHz yielded quantitatively similar behavior (allowing for the expected change in beam waist radius with frequency). The excellent azimuthal symmetry of the beam is clear. The beam amplitude is Gaussian out to $r = 5$ mm, though sidelobes become evident outside that radius at $|S_{21}| = 0.2$, or 4% (-14 dB) in power. We measure beam waist radii of 3.8 mm and 3.7 mm in X and Y , respectively, in agreement with expectations given the scatter in the measurement (see Figure 13). We see that the phase is fairly flat (< 0.5 rad) out to $r = 5$ mm, but it increases to about 1 radian (approximately 0.17 mm optical path length at 275 GHz) by $r = 10$ mm. In Gaussian optics, we expect the phase front to be flat. It is not possible to explain this deviation simply by the uncertainty in locating the beam waist because the Gaussian optics phase front radius of curvature does not

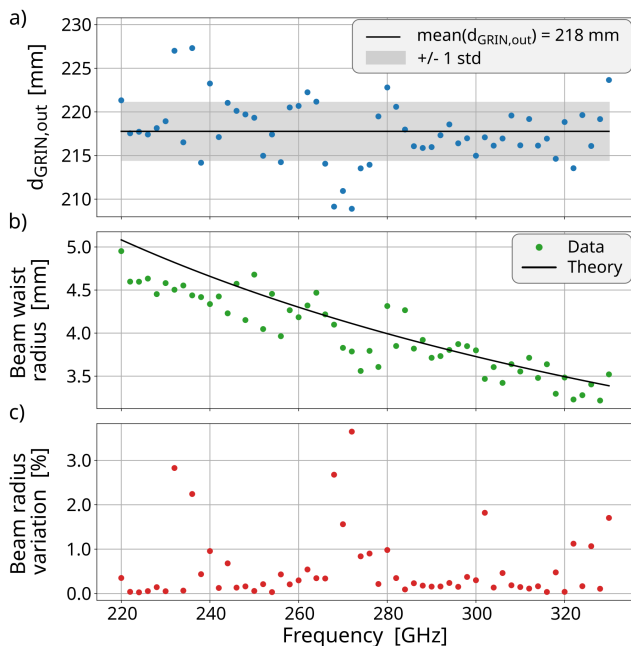


Fig. 13. a) Distance between the GRIN lens and the beam waist, $d_{GRIN,out}$, as a function of frequency; b) dependence of the beam waist radius on frequency; and, c) percentage difference between the beam radius at $f_{GRIN,out} = 218$ mm and the beam waist radius for each frequency. The sharp excursions in the latter at specific frequencies are likely due to standing waves, which suggests they are also responsible for the large excursions in $d_{GRIN,out}$.

evolve quickly enough: the implied value, $R = 300$ mm, requires a displacement of $\Delta Z = 7$ mm from the beam waist, much larger than the uncertainty on $\langle d_{GRIN,out}(f) \rangle$ seen in Figure 13. We note the phase has an oscillatory structure similar to the sidelobes, suggesting a common origin. We observe other features, such as an asymmetry in beam radius as a function of distance from the post-lens beam waist, that Gaussian optics also cannot explain. The sidelobes and phase front curvature thus likely result from deviations of the system from ideal Gaussian optics. The reflections discussed below are a possible cause.

3) *Transmittance*: We measured the transmittance of the lens as a function of frequency by integrating the power in beam maps with and without the lens at the nominal beam waist position and taking their ratio (see Figure 15). The transmittance varies between 75% and 100% over the frequency range measured, with an average of 91%. This result is a significant improvement over a conventional curved silicon lens without AR treatment, which would have a transmittance of only 49% (assuming no constructive/destructive interference given the absence of parallel surfaces).

The performance is, however, clearly non-ideal, with oscillatory behavior suggestive of standing waves. We repeated the measurement at three, randomly chosen locations along the optical axis between 20 mm and 70 mm before the nominal beam waist and see consistent behavior, indicating the standing waves are not between the lens and the beam-mapper but are likely internal to the lens. There are two standing wave periods: one ≈ 100 GHz and the other 8–9 GHz. Motivated

by the known gaps between wafers, we interpret these fringe periods using a simple model for transmission through a slab of thickness t and uniform index n situated in air.

For the 100 GHz period, we observe transmittance maxima at 215–220 GHz and 310–320 GHz and a transmittance minimum at 270–275 GHz. The absolute frequencies and the frequency spacing of these extrema are consistent with the model for $t = 0.525$ mm (i.e., the single wafer thickness) and $\langle n \rangle \approx 2.6$ –2.7. This value is too high to be explained by the AR wafer ($n_{AR} = 1.21$ –2.54). It is also somewhat higher than $\langle n_{GRIN} \rangle = 2.99$ calculated in Section II-C but perhaps explicable if a different radial weighting is appropriate. The 100 GHz period is thus mostly likely explained by the known gaps between the GRIN wafers.

The 8–9 GHz period is more challenging to understand. The model implies this smaller period corresponds to a larger t , and the only available thicknesses are those of the entire lens including AR layers (3.765 mm), the GRIN wafer stack alone (2.625 mm), and the GRIN wafer stack plus one AR wafer (3.15 mm). (Subsets of the GRIN wafer stack would yield t values too small.) Quantitatively, however, $\langle n \rangle t \approx 17$ –19 mm for this period, requiring far too large a value of $\langle n \rangle$ for all these candidate t values.

On closer inspection, one notices that the extremum transmittance values do not vary monotonically with frequency; rather, the peak-to-peak transmittance variation seems to alternate between consecutive maxima or minima. This variation suggests two overlapping interference patterns, each with 16–18 GHz period, displaced by about half that amount. For this model, the three candidate thicknesses yield $\langle n \rangle \approx 2.2$ –2.5 (entire lens), $\langle n \rangle \approx 3.2$ –3.6 (GRIN wafers alone), and $\langle n \rangle \approx 2.6$ –3.0 (GRIN wafers plus one AR wafer). While the first and last $\langle n \rangle$ ranges are acceptably consistent with the range inferred from the 100 GHz period analysis, the latter model seems a better match. More importantly, it provides a mechanism for two overlapping interference patterns: if the two possible realizations (GRIN + input side AR, GRIN + output side AR) have mean indices differing by only 4%, then their interference patterns will differ in frequency by that percentage, while the corresponding difference in period (4% of 16–18 GHz is ≈ 0.7 GHz) would not be evident in Figure 15. Lastly, this model may explain the non-monotonicity of the extremum transmittances by corresponding differences between the two realizations for the air-silicon index mismatch, which sets the amplitude of the interference pattern.

In prior work [32], we etched two-layer AR treatments into one face of each of two silicon wafers, leaving the other faces of both wafers unpatterned, and mated the unetched faces together. We cleaned these mating surfaces using techniques and tools usually employed as preparation for wafer bonding, in particular an automated particle mapper to find and remove debris. The resulting transmittance was $>99\%$, indicating no gap. Such particle mappers are not natively able to process patterned surfaces, however. Furthermore, an attempt (parallel to this work) to mate four-layer AR-structured wafers (patterned from both sides as done here) to bulk silicon wafers also displayed sub-design reflectance performance attributable to gaps. Post-measurement inspection revealed photoresist

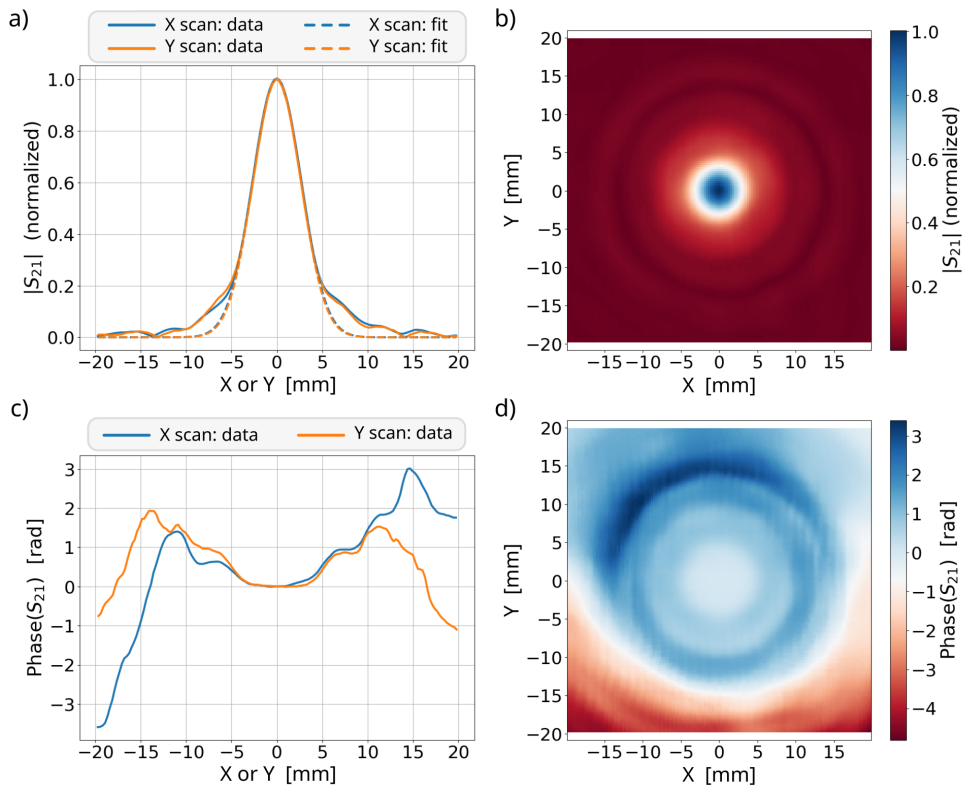


Fig. 14. Beam map at the beam waist of the GRIN lens at 275 GHz. a), b) Peak-normalized electric field magnitude $|S_{21}|$; c), d) electric field phase relative to its value on the optical axis. a), c) show 1D scans along X (at $Y = 0$) and Y (at $X = 0$).

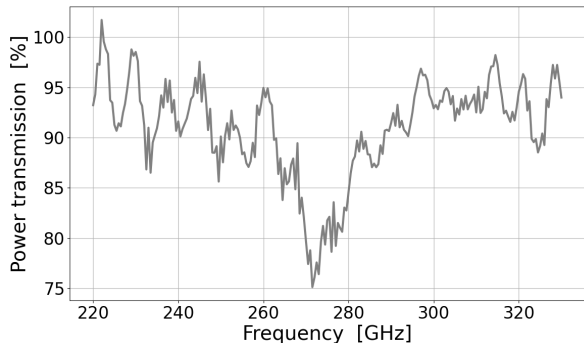


Fig. 15. Power transmission of the GRIN lens measured between 220 GHz and 330 GHz. The measurement was obtained by mapping the beam with and without the lens at 221 frequency points, and calculating the integrated transmitted power ratio between the two beam maps. The same measurement was repeated three times at different Z locations and averaged to reduce the white noise and potential standing wave effects.

residue, small pieces of silicon left due to broken posts, and other debris, all of which interfered with wafer mating. We suspect the same type of debris here. We plan to undertake more aggressive chemical cleaning efforts in the future and will also seek out facilities for particle mapping in the presence of a periodic etched pattern.

V. CONCLUSION

We have successfully demonstrated a gradient index lens in silicon constructed using DRIE-patterned sub-wavelength

structures. The lens incorporates a similarly structured, three-layer anti-reflection treatment designed for a bandwidth of 160–355 GHz (1:2.2). We measured the focal length of the lens over the frequency range 220–330 GHz to be 218 mm, 20 mm shorter than the design value. We attribute this discrepancy to a slight over-etching of the holes, reaching about $1 \mu\text{m}$ at the edge of the lens. Over the same frequency range, the beam profile is close to Gaussian. The overall transmittance of the lens over this frequency range varies between 75% and 100%, a significant improvement over the mean 49% expected for two untreated air-silicon interfaces. Overall, this work is an important first step toward broad-bandwidth optical elements using silicon at millimeter and submillimeter wavelengths, and the DRIE approach is viable up to THz frequencies. Our eventual goal is elements 300 mm in diameter with up to 5.25:1 bandwidth.

Some non-idealities are present, motivating future work. The transmittance is appreciably below expectations and shows a dependence on frequency suggestive of small gaps between the wafers. It is plausible these gaps arise from insufficient cleaning of etching residue and debris. Sidelobes and phase deviations from expectations appear below $|S_{21}| \approx 0.2$ (4% or -14 dB relative to peak power), indicating deviations from ideal Gaussian optics. The known wafer gaps may be the cause, though it is possible that there are other contributors, too.

In addition to addressing gaps between the wafers, future work will include: stacking of more wafers to shorten the focal length; testing a second iteration over a broader frequency

range; increasing the number of layers in the anti-reflection structure to broaden the bandwidth; and, increasing the wafer diameter.

FUNDING

This work has been supported by the Caltech-JPL President's and Director's Research and Development Fund and the National Aeronautics and Space Administration under awards NNX15AE01G and 80NSSC20K0655. T. Macioce acknowledges support from a NASA Space Technology Research Fellowship, award 80NSSC18K1167. C. J-K., J. G., S. R., and F. D. carried out research/fabrication at the Jet Propulsion Laboratory, operated by the California Institute of Technology under a contract with the National Aeronautics and Space Administration (80NM0018D0004).

ACKNOWLEDGMENT

We performed this work at the California Institute of Technology and the MicroDevices Laboratory of the Jet Propulsion Laboratory (operated by the California Institute of Technology under a contract with the National Aeronautics and Space Administration). The authors thank S. J. E. Radford and H. Yoshida for early pathfinding work and P. Goldsmith for his comments on Gaussian beam optics and suggestions about GRIN lens characterization.

REFERENCES

- [1] A. J. Gatesman, J. Waldman, M. Ji, C. Musante, and S. Yagvesson, "An anti-reflection coating for silicon optics at terahertz frequencies," *IEEE Microwave and Guided Wave Letters*, vol. 10, pp. 264–266, 2000.
- [2] J. Lau, J. Fowler, T. Marriage, L. Page, J. Leong, E. Wishnow, R. Henry, E. Wollack, M. Halpern, D. Marsden, and G. Marsden, "Millimeter-wave antireflection coating for cryogenic silicon lenses," *Appl. Opt.*, vol. 45, pp. 3746–3751, 2006.
- [3] D. Rosen, A. Suzuki, B. Keating, W. Krantz, A. T. Lee, E. Quealy, P. L. Richards, P. Siritanasak, and W. Walker, "Epoxy-based broadband antireflection coating for millimeter-wave optics," *Appl. Opt.*, vol. 52, pp. 8102–8105, 2013.
- [4] O. Jeong, A. Lee, C. Raum, and A. Suzuki, "Broadband Plasma-Sprayed Anti-reflection Coating for Millimeter-Wave Astrophysics Experiments," *Journal of Low Temperature Physics*, vol. 184, pp. 621–626, Aug. 2016.
- [5] J. Zhang, P. A. R. Ade, P. Mauskopf, L. Moncelsi, G. Savini, and N. Whitehouse, "New artificial dielectric metamaterial and its application as a terahertz antireflection coating," *Appl. Opt.*, vol. 48, p. 6635, Dec. 2009.
- [6] P. Moseley, G. Savini, J. Zhang, and P. Ade, "Dual focus polarisation splitting lens," *Optics Express*, vol. 25, no. 21, pp. 25363–25373, 2017.
- [7] R. Datta, C. D. Munson, M. D. Niemack, J. J. McMahon, J. Britton, E. J. Wollack, J. Beall, M. J. Devlin, J. Fowler, P. Gallardo, J. Hubmayr, K. Irwin, L. Newburgh, J. P. Nibarger, L. Page, M. A. Quijada, B. L. Schmitt, S. T. Staggs, R. Thornton, and L. Zhang, "Large-aperture wide-bandwidth antireflection-coated silicon lenses for millimeter wavelengths," *Appl. Opt.*, vol. 52, pp. 8747–8758, 2013.
- [8] R. J. Thornton, P. A. R. Ade, S. Aiola, F. E. Angilè, M. Amiri, J. A. Beall, D. T. Becker, H. M. Cho, S. K. Choi, P. Corlies, K. P. Coughlin, R. Datta, M. J. Devlin, S. R. Dicker, R. Dünner, J. W. Fowler, A. E. Fox, P. A. Gallardo, J. Gao, E. Grace, M. Halpern, M. Hasselfield, S. W. Henderson, G. C. Hilton, A. D. Hincks, S. P. Ho, J. Hubmayr, K. D. Irwin, J. Klein, B. Koopman, D. Li, T. Louis, M. Lungu, L. Maurin, J. McMahon, C. D. Munson, S. Naess, F. Nati, L. Newburgh, J. Nibarger, M. D. Niemack, P. Niraula, M. R. Nolta, L. A. Page, C. G. Pappas, A. Schillaci, B. L. Schmitt, N. Sehgal, J. L. Sievers, S. M. Simon, S. T. Staggs, C. Tucker, M. Uehara, J. van Lanen, J. T. Ward, and E. J. Wollack, "The Atacama Cosmology Telescope: The Polarization-sensitive ACTPol Instrument," *The Astrophysical Journal Supplement Series*, vol. 227, pp. 21/1–15, 2016.
- [9] S. W. Henderson, R. Allison, J. Austerermann, T. Baildon, N. Battaglia, J. A. Beall, D. Becker, F. De Bernardis, J. R. Bond, E. Calabrese, S. K. Choi, K. P. Coughlin, K. T. Crowley, R. Datta, M. J. Devlin, S. M. Duff, J. Dunkley, R. Dünner, A. van Engelen, P. A. Gallardo, E. Grace, M. Hasselfield, F. Hills, G. C. Hilton, A. D. Hincks, R. Hložek, S. P. Ho, J. Hubmayr, K. Huffenberger, J. P. Hughes, K. D. Irwin, B. J. Koopman, A. B. Kosowsky, D. Li, J. McMahon, C. Munson, F. Nati, L. Newburgh, M. D. Niemack, P. Niraula, L. A. Page, C. G. Pappas, M. Salatino, A. Schillaci, B. L. Schmitt, N. Sehgal, B. D. Sherwin, J. L. Sievers, S. M. Simon, D. N. Spergel, S. T. Staggs, J. R. Stevens, R. Thornton, J. Van Lanen, E. M. Vavagiakis, J. T. Ward, and E. J. Wollack, "Advanced ACTPol Cryogenic Detector Arrays and Readout," *Journal of Low Temperature Physics*, vol. 184, pp. 772–779, 2016.
- [10] G. W. Wilson, S. Abi-Saad, P. Ade, I. Aretxaga, J. Austerermann, Y. Ban, J. Bardin, J. Beall, M. Berthoud, S. Bryan, J. Bussan, E. Castillo, M. Chavez, R. Contente, N. S. DeNigris, B. Dober, M. Eiben, D. Ferrusca, L. Fissel, J. Gao, J. E. Golec, R. Golina, A. Gomez, S. Gordon, R. Guteruth, G. Hilton, N. Hosseini, J. Hubmayr, D. Hughes, S. Kuczarski, D. Lee, E. Lunde, Z. Ma, H. Mani, P. Mauskopf, M. McCrackan, C. McKenney, J. McMahon, G. Novak, G. Pisano, A. Pope, A. Ralston, I. Rodriguez, D. Sánchez-Argüelles, F. P. Schloerb, S. Simon, A. Sinclair, K. Soucar, A. Torres Campos, C. Tucker, J. Ullom, E. Van Camp, J. Van Lanen, M. Velazquez, M. Vissers, E. Weeks, and M. S. Yun, "The TolTEC camera: an overview of the instrument and in-lab testing results," in *Millimeter, Submillimeter, and Far-Infrared Detectors and Instrumentation for Astronomy X*, ser. Society of Photo-Optical Instrumentation Engineers (SPIE) Conference Series, J. Zmuidzinas and J.-R. Gao, Eds., vol. 11453. Bellingham, WA: SPIE Press, Dec. 2020, pp. 1145302/1–20.
- [11] J. E. Golec, J. J. McMahon, A. Ali, S. Dicker, N. Galitzki, K. Harrington, B. Westbrook, E. J. Wollack, Z. Xu, and N. Zhu, "Design and fabrication of metamaterial anti-reflection coatings for the Simons Observatory," in *Advances in Optical and Mechanical Technologies for Telescopes and Instrumentation IV*, ser. Society of Photo-Optical Instrumentation Engineers (SPIE) Conference Series, R. Navarro and R. Geyl, Eds., vol. 11451. Bellingham, WA: SPIE Press, 2020, pp. 114515T/1–8.
- [12] N. Zhu, T. Bhandarkar, G. Coppi, A. M. Kofman, J. L. Orlowski-Scherer, Z. Xu, S. Adachi, P. Ade, S. Aiola, J. Austerermann, A. O. Bazarko, J. A. Beall, S. Bhimani, J. R. Bond, G. E. Chesmore, S. K. Choi, J. Connors, N. F. Cothard, M. Devlin, S. Dicker, B. Dober, C. J. Duell, S. M. Duff, R. Dünner, G. Fabbian, N. Galitzki, P. A. Gallardo, J. E. Golec, S. K. Haridas, K. Harrington, E. Healy, S.-P. P. Ho, Z. B. Huber, J. Hubmayr, J. Iuliano, B. R. Johnson, B. Keating, K. Kiuchi, B. J. Koopman, J. Lashner, A. T. Lee, Y. Li, M. Limon, M. Link, T. J. Lucas, H. McCarrick, J. Moore, F. Nati, L. B. Newburgh, M. D. Niemack, E. Pierpaoli, M. J. Randall, K. P. Sarmiento, L. J. Saunders, E. Seibert, C. Sierra, R. Sonka, J. Spisak, S. Sutariya, O. Tajima, G. P. Teply, R. J. Thornton, T. Tsan, C. Tucker, J. Ullom, E. M. Vavagiakis, M. R. Vissers, S. Walker, B. Westbrook, E. J. Wollack, and M. Zannoni, "The Simons Observatory Large Aperture Telescope Receiver," *The Astrophysical Journal Supplement Series*, vol. 256, pp. 23/1–20, 2021.
- [13] A. J. Anderson, P. Barry, A. N. Bender, B. A. Benson, L. E. Bleem, J. E. Carlstrom, T. W. Cecil, C. L. Chang, T. M. Crawford, K. R. Dibert, M. A. Dobbs, K. Fichman, N. W. Halverson, W. L. Holzapfel, A. Hryciuk, K. S. Karkare, J. Li, M. Lisovenko, D. Marrone, J. McMahon, J. Montgomery, T. Natoli, Z. Pan, S. Raghunathan, C. L. Reichardt, M. Rouble, E. Shirokoff, G. Smecher, A. A. Stark, J. D. Vieira, and M. R. Young, "SPT-3G+: mapping the high-frequency cosmic microwave background using kinetic inductance detectors," in *Millimeter, Submillimeter, and Far-Infrared Detectors and Instrumentation for Astronomy XI*, ser. Society of Photo-Optical Instrumentation Engineers (SPIE) Conference Series, J. Zmuidzinas and J.-R. Gao, Eds., vol. 12190. Bellingham, WA: SPIE Press, 2022, pp. 1219003/1–26.
- [14] N. F. Cothard, S. K. Choi, C. J. Duell, T. Herter, J. Hubmayr, J. McMahon, M. D. Niemack, T. Nikola, C. Sierra, G. J. Stacey, E. M. Vavagiakis, E. J. Wollack, and B. Zou, "The Design of the CCAT-prime Epoch of Reionization Spectrometer Instrument," *Journal of Low Temperature Physics*, vol. 199, no. 3-4, pp. 898–907, 2020.
- [15] E. M. Vavagiakis, C. J. Duell, J. Austerermann, J. Beall, T. Bhandarkar, S. C. Chapman, S. K. Choi, G. Coppi, S. Dicker, M. Devlin, R. G. Freundt, J. Gao, C. Groppi, T. L. Herter, Z. B. Huber, J. Hubmayr, D. Johnstone, B. Keller, A. M. Kofman, Y. Li, P. Mauskopf, J. McMahon, J. Moore, C. C. Murphy, M. D. Niemack, T. Nikola, J. Orlowski-Scherer, K. M. Rossi, A. K. Sinclair, G. J. Stacey, J. Ullom, M. Vissers, J. Wheeler, Z. Xu, N. Zhu, and B. Zou, "CCAT-prime: design of the Mod-Cam receiver and 280 GHz MKID instrument module," in *Millimeter, Submillimeter, and Far-Infrared Detectors and Instrumentation for*

- Astronomy XI*, ser. Society of Photo-Optical Instrumentation Engineers (SPIE) Conference Series, J. Zmuidzinas and J.-R. Gao, Eds., vol. 12190. Bellingham, WA: SPIE Press, 2022, p. 1219004.
- [16] P. A. Gallardo, B. Benson, J. Carlstrom, S. R. Dicker, N. Emerson, J. E. Gudmundsson, R. Hills, M. Limon, J. McMahon, M. D. Niemack, J. M. Nagy, S. Padin, J. Ruhl, and S. M. Simon, "Optical design concept of the CMB-S4 large-aperture telescopes and cameras," in *Millimeter, Submillimeter, and Far-Infrared Detectors and Instrumentation for Astronomy XI*, ser. Society of Photo-Optical Instrumentation Engineers (SPIE) Conference Series, J. Zmuidzinas and J.-R. Gao, Eds., vol. 12190. Bellingham, WA: SPIE Press, 2022, pp. 121900C/1–14.
- [17] K. P. Coughlin, J. J. McMahon, K. T. Crowley, B. J. Koopman, K. H. Miller, S. M. Simon, and E. J. Wollack, "Pushing the Limits of Broadband and High-Frequency Metamaterial Silicon Antireflection Coatings," *Journal of Low Temperature Physics*, vol. 193, pp. 876–885, 2018.
- [18] K. Young, Q. Wen, S. Hanany, H. Imada, J. Koch, T. Matsumura, O. Suttman, and V. Schütz, "Broadband millimeter-wave anti-reflection coatings on silicon using pyramidal sub-wavelength structures," *Journal of Applied Physics*, vol. 121, no. 21, p. 213103, Jun. 2017.
- [19] T. Nitta, Y. Sekimoto, K. Noda, S. Sekiguchi, S. Shu, H. Matsuo, A. Dominjon, M. Naruse, N. Kuno, and N. Nakai, "Broadband Pillar-Type Antireflective Subwavelength Structures for Silicon and Alumina," *IEEE Transactions on Terahertz Science and Technology*, vol. 7, pp. 295–301, 2017.
- [20] T. Nitta, Y. Sekimoto, T. Hasebe, K. Noda, S. Sekiguchi, M. Nagai, S. Hattori, Y. Murayama, H. Matsuo, A. Dominjon, W. Shan, M. Naruse, N. Kuno, and N. Nakai, "Design, Fabrication and Measurement of Pyramid-Type Antireflective Structures on Columnar Crystal Silicon Lens for Millimeter-Wave Astronomy," *Journal of Low Temperature Physics*, vol. 193, pp. 976–983, 2018.
- [21] T.-H. Her, R. J. Finlay, C. Wu, S. Deliwala, and E. Mazur, "Microstructuring of silicon with femtosecond laser pulses," *Applied Physics Letters*, vol. 73, p. 1673, Sep. 1998.
- [22] C. Y. Drouët d'Aubigny, C. K. Walker, and B. D. Jones, "Laser microchemical etching of waveguides and quasi-optical components," in *Micromachining and Microfabrication Process Technology VII*, ser. Proceedings of SPIE, J. M. Karam and J. Yasaitis, Eds., vol. 4557. Bellingham, WA: SPIE, Sep. 2001, pp. 101–110.
- [23] J. Bueno, S. Bosma, T. Buskamp-Alda, M. Alonso-delPino, and N. Lombart, "Lossless Matching Layer for Silicon Lens Arrays at 500 GHz Using Laser Ablated Structures," *IEEE Transactions on Terahertz Science and Technology*, vol. 12, no. 6, pp. 667–672, 2022.
- [24] N. Farias, S. Beckman, A. T. Lee, and A. Suzuki, "Simulated Performance of Laser-Machined Metamaterial Anti-reflection Coatings," *Journal of Low Temperature Physics*, vol. 209, pp. 1232–1241, 2022.
- [25] C. Jung-Kubiak et al., "A Multi-Step DRIE Process for Complex Terahertz Waveguide Components," *IEEE Transactions on Terahertz Science and Technology*, vol. 6, no. 5, pp. 390–395, 2016.
- [26] P. A. Gallardo, B. J. Koopman, N. F. Cothard, S. M. M. Bruno, G. Cortes-Medellin, G. Marchetti, K. H. Miller, B. Mockler, M. D. Niemack, G. Stacey, and E. J. Wollack, "Deep reactive ion etched anti-reflection coatings for sub-millimeter silicon optics," *Appl. Opt.*, vol. 56, p. 2796, Apr. 2017.
- [27] J. D. Wheeler, B. Koopman, P. Gallardo, P. R. Maloney, S. Brugger, G. Cortes-Medellin, R. Datta, C. D. Dowell, J. Glenn, S. Golwala, C. McKenney, J. J. McMahon, C. D. Munson, M. Niemack, S. Parshley, and G. Stacey, "Antireflection coatings for submillimeter silicon lenses," in *Millimeter, Submillimeter, and Far-Infrared Detectors and Instrumentation for Astronomy VII*, ser. Proceedings of SPIE, vol. 9153. Bellingham, WA: SPIE, 2014, pp. 91532Z/1–11.
- [28] T. Wada, H. Makitsubo, and M. Mita, "Mono-Material Multilayer Interference Optical Filter with Sub-Wavelength Structure for Infrared and Terahertz Optics," *Applied Physics Express*, vol. 3, no. 10, p. 102503, Oct. 2010.
- [29] A. Wagner-Gentner, U. U. Graf, D. Rabanus, and K. Jacobs, "Low loss THz window," *Infrared Physics and Technology*, vol. 48, pp. 249–253, Aug. 2006.
- [30] K.-F. Schuster, N. Krebs, Y. Guillaud, F. Mattiocco, M. Kornberg, and A. Poglitsch, "Micro-machined quasi-optical Elements for THz Applications," in *Sixteenth International Symposium on Space Terahertz Technology*, pp. 524–528, May 2005, <http://adsabs.harvard.edu/abs/2005stt..conf..524S>.
- [31] C. Brückner, T. Käsebier, B. Pradarutti, S. Riehemann, G. Notni, E.-B. Kley, and A. Tünnermann, "Broadband antireflective structures applied to high resistive float zone silicon in the THz spectral range," *Optics Express*, vol. 17, pp. 3063–3077, 2009. [Online]. Available: <http://www.opticsexpress.org/abstract.cfm?URI=oe-17-5-3063>
- [32] F. Defrance, C. Jung-Kubiak, J. Sayers, J. Connors, C. deYoung, M. I. Hollister, H. Yoshida, G. Chattopadhyay, S. R. Golwala, and S. J. E. Radford, "1.6:1 bandwidth two-layer antireflection structure for silicon matched to the 190-310 GHz atmospheric window," *Appl. Opt.*, vol. 57, no. 18, pp. 5196–5209, Jun 2018. [Online]. Available: <https://opg.optica.org/ao/abstract.cfm?URI=ao-57-18-5196>
- [33] M. Nagai, S. Ezaki, R. Sakai, K. Kaneko, H. Imada, T. Kojima, W. Shan, Y. Uzawa, and S. Asayama, "Optical measurements of the silicon vacuum window with anti-reflective sub-wavelength structure for ASTE Band 10," *Appl. Opt.*, vol. 62, pp. 6287–6296, Aug. 2023.
- [34] T. Hasebe, T. Hayashi, H. Takakura, Y. Sekimoto, K. Ishikawa, Y. Shohmitsu, K. Noda, S. Saeki, Y. Ezoe, and T. Nitta, "Development of Multi-Layer Anti-Reflection Structures for Millimeter-Wave Silicon Optics Using Deep Reactive Ion Etching Process," *Journal of Low Temperature Physics*, vol. 199, no. 1-2, pp. 339–347, 2020.
- [35] T. Hasebe, T. Hayashi, Y. Shohmitsu, T. Nitta, H. Matsuo, and Y. Sekimoto, "Fabrication of three-layer silicon antireflection structures in 200-450 GHz using deep reactive ion etching," *Appl. Opt.*, vol. 60, p. 10462, 2021.
- [36] F. Defrance, C. Jung-Kubiak, S. Rahiminejad, T. Macioce, J. Sayers, J. Connors, S. J. E. Radford, G. Chattopadhyay, and S. R. Golwala, "Flat low-loss silicon gradient index lens for millimeter and submillimeter wavelengths," *Journal of Low Temperature Physics*, vol. 199, no. 1, pp. 376–383, Apr 2020. [Online]. Available: <https://doi.org/10.1007/s10909-019-02255-x>
- [37] R. W. Wood, *Physical Optics*. Macmillan, New York, 1905.
- [38] J. B. Caldwell, "Optical design with wood lenses I: infinite conjugate systems," *Appl. Opt.*, vol. 31, no. 13, pp. 2317–2325, May 1992. [Online]. Available: <https://opg.optica.org/ao/abstract.cfm?URI=ao-31-13-2317>
- [39] W. N. Charman, "Gradient-index optics," *Canadian Journal of Optometry*, vol. 44, no. 4, p. 8, Dec. 1982. [Online]. Available: <https://openjournals.uwaterloo.ca/index.php/cjo/article/view/4245>
- [40] G. Savini, P. A. Ade, and J. Zhang, "A new artificial material approach for flat thz frequency lenses," *Opt. Express*, vol. 20, no. 23, pp. 25766–25773, Nov 2012. [Online]. Available: <https://opg.optica.org/oe/abstract.cfm?URI=oe-20-23-25766>
- [41] D. J. Fischer, C. J. Harkrider, and D. T. Moore, "Design and manufacture of a gradient-index axicon," *Appl. Opt.*, vol. 39, no. 16, pp. 2687–2694, Jun 2000. [Online]. Available: <https://opg.optica.org/ao/abstract.cfm?URI=ao-39-16-2687>
- [42] V. Nguyen, S. Larouche, N. Landy, J. S. Lee, and D. R. Smith, "Quantitative comparison of gradient index and refractive lenses," *J. Opt. Soc. Am. A*, vol. 29, no. 11, pp. 2479–2497, Nov 2012. [Online]. Available: <https://opg.optica.org/josaa/abstract.cfm?URI=josaa-29-11-2479>
- [43] A. Mikaelian and A. Prokhorov, "V self-focusing media with variable index of refraction," in *Progress in Optics*, E. Wolf, Ed. Elsevier, 1980, vol. 17, pp. 279–345. [Online]. Available: <https://www.sciencedirect.com/science/article/pii/S0079663808702415>
- [44] J. Bor, B. Fuchs, O. Lafond, and M. Himdi, "Design and characterization of a foam-based mikaelian lens antennas in millimeter waves," *International Journal of Microwave and Wireless Technologies*, vol. 7, no. 6, p. 769–773, 2015.
- [45] X. Su, A. N. Norris, C. W. Cushing, M. R. Haberman, and P. S. Wilson, "Broadband focusing of underwater sound using a transparent pentamode lens," *The Journal of the Acoustical Society of America*, vol. 141, no. 6, pp. 4408–4417, 06 2017. [Online]. Available: <https://doi.org/10.1121/1.4985195>
- [46] A. D. Falco, S. C. Kehr, and U. Leonhardt, "Luneburg lens in silicon photonics," *Opt. Express*, vol. 19, no. 6, pp. 5156–5162, Mar 2011. [Online]. Available: <https://opg.optica.org/oe/abstract.cfm?URI=oe-19-6-5156>
- [47] Y. Zhou, J. Li, W. Xiao, and H. Chen, "Broadband achromatic aberration general conformal luneburg lens with quasi-far-field highly efficient super-focusing," *Opt. Lett.*, vol. 47, no. 15, pp. 3820–3823, Aug 2022. [Online]. Available: <https://opg.optica.org/ol/abstract.cfm?URI=ol-47-15-3820>
- [48] S. Manafi, J. F. González, and D. S. Filipovic, "Design of a perforated flat luneburg lens antenna array for wideband millimeter-wave applications," in *2019 13th European Conference on Antennas and Propagation (EuCAP)*, 2019, pp. 1–5.
- [49] T. Macioce, F. Defrance, C. Jung-Kubiak, S. Rahiminejad, J. Sayers, J. Connors, G. Chattopadhyay, S. R. Golwala, and S. J. E. Radford, "Multilayer Etched Antireflective Structures for Silicon Vacuum Win-

- dows," *Journal of Low Temperature Physics*, vol. 199, no. 3-4, pp. 935–942, May 2020.
- [50] R. E. Collin, "Theory and design of wide-band multisection quarter-wave transformers," *Proceedings of the IRE*, vol. 43, no. 2, pp. 179–185, 1955.
- [51] D. M. Pozar, *Microwave Engineering*. New York, NY: John Wiley, 2011.
- [52] S. Orfanidis, "A two-section dual-band chebyshev impedance transformer," *IEEE Microwave and Wireless Components Letters*, vol. 13, no. 9, pp. 382–384, 2003.
- [53] S. J. Orfanidis, *Electromagnetic Waves and Antennas*. Rutgers University New Brunswick, NJ, 2016. [Online]. Available: <http://eceweb1.rutgers.edu/~orfanidi/ewa/>
- [54] A. MacKay, "Proof of polarisation independence and nonexistence of crosspolar terms for targets presenting n-fold ($n \geq 2$) rotational symmetry with special reference to frequency-selective surfaces," *Electronics Letters*, vol. 25, no. 24, p. 1624, 1989.
- [55] J. Krupka, J. Breeze, A. Centeno, N. Alford, T. Claussen, and L. Jensen, "Measurements of permittivity, dielectric loss tangent, and resistivity of float-zone silicon at microwave frequencies," *IEEE Transactions on Microwave Theory and Techniques*, vol. 54, no. 11, pp. 3995–4001, 2006.
- [56] J. Krupka, P. Kamiński, and L. Jensen, "High q-factor millimeter-wave silicon resonators," *IEEE Transactions on Microwave Theory and Techniques*, vol. 64, no. 12, pp. 4149–4154, 2016.
- [57] J. Krupka, P. Kamiński, R. Kozłowski, B. Surma, A. Dierlamm, and M. Kwestarz, "Dielectric properties of semi-insulating silicon at microwave frequencies," *Applied Physics Letters*, vol. 107, no. 8, p. 082105, 08 2015. [Online]. Available: <https://doi.org/10.1063/1.4929503>
- [58] V. V. Parshin, R. Heidinger, B. A. Andreev, A. V. Gusev, and V. B. Shmagin, "Silicon as an advanced window material for high power gyrotrons," *International Journal of Infrared and Millimeter Waves*, vol. 16, no. 5, pp. 863–877, May 1995. [Online]. Available: <https://doi.org/10.1007/BF02066662>
- [59] W. R. Thurber, D. C. Lewis, and W. M. Bullis, "Resistivity and carrier lifetime in gold-doped silicon," 1973. [Online]. Available: <https://api.semanticscholar.org/CorpusID:136053534>
- [60] P. F. Goldsmith, *Quasioptical Systems : Gaussian Beam Quasioptical Propagation and Applications*. Wiley-IEEE Press, 1998.

APPENDIX A

DEMONSTRATION THAT A LOW-POWER PARABOLIC WOOD LENS IS FREE OF SPHERICAL ABERRATION; RELATION BETWEEN FOCAL LENGTH AND WOOD LENS PARAMETERS

For an optic to be free of spherical aberration, it must transform an incoming flat isophase surface (surface of constant phase) to a perfectly spherical isophase surface of radius f centered on the focal point. To be more precise, it must yield a total optical path length ($OPL = \text{phase delay} \times \lambda_0/2\pi$ where λ_0 is the wavelength in the external medium of refractive index n_0) between these two isophase surfaces that is independent of r .

The total OPL between the incoming flat and outgoing spherical isophase surfaces in Figure 3 is

$$OPL_{total} = OPL_{GRIN} + OPL_0 \quad (21)$$

$$= t n(r) + \left[\sqrt{r^2 + f^2} - f \right] n_0 \quad (22)$$

The first term is the OPL through the lens, which is fixed at t in physical path length but varies in OPL with r due to $n(r)$. The second term is the OPL in the medium n_0 , at transverse radius r , between the output lens surface and the spherical isophase surface of radius f centered on the focal point; see Figure 3 for the geometry, including the right triangle with sides f and r .

If we then require OPL_{total} to be constant and to take on the on-axis value of $t n(0)$, we obtain

$$t n(0) = t n(r) + \left[\sqrt{r^2 + f^2} - f \right] n_0 \quad (23)$$

which we may use to solve for $n(r)$:

$$n(r) = n(0) - n_0 \frac{f}{t} \left[\sqrt{1 + \frac{r^2}{f^2}} - 1 \right] \quad (24)$$

The above index profile yields no spherical aberration, but does not provide the power-law profile of a Wood lens.

For a low-power lens, $r \ll f$ (equivalent to the paraxial approximation) and we may Taylor expand the square root to first order in r^2/f^2 , yielding

$$n(r) \approx n(0) - \frac{n_0}{2} \frac{r^2}{f t} \quad (25)$$

This $n(r)$ function is a second-order Wood lens (Equation 2); that is, the index gradient is parabolic. For this type of lens, we may solve for f in terms of transverse radius R and maximum and minimum refractive indices $n_{max} = n(0)$ and $n_{min} = n(R)$:

$$f \approx n_0 \frac{R^2}{2t(n_{max} - n_{min})} \quad (26)$$

The GRIN lens demonstrated in this paper has $R = 40$ mm and an expected focal length $f = 238$ mm. Thus, the parameter describing the fractional error in the Taylor expansion, $x^2 = (r^2/f^2)^2$, satisfies $x^2 < 0.0008 \ll 1$: the low-power/paraxial approximation is satisfied to high precision. As $x = r^2/f^2$ increases, spherical aberration will become larger because the accuracy with which a parabolic index profile yields a spherical phase front degrades. It is clear

from the above approximation that spherical aberration can be reduced by including more terms in the Taylor expansion to obtain a higher-order Wood lens, but, as noted in Section II-A, such designs suffer coma [38]. Section II-A summarizes other approaches that are preferable.

APPENDIX B

EXACT ISOPHASE SURFACE OF A PARABOLIC WOOD LENS

It is reasonable to surmise that a parabolic Wood lens yields a parabolic isophase surface. A straightforward calculation, analogous to the one done above, demonstrates this fact. Instead of specifying the shape of the isophase surface, we leave it to be determined as the function $OPL_0(r)$:

$$OPL_{total} = OPL_{GRIN} + OPL_0(r) \quad (27)$$

If we again require $OPL_{total} = t n(0)$ and $OPL_{GRIN} = t n(r)$, we find

$$OPL_0(r) = t [n(0) - n(r)] = \frac{n_0}{2} \frac{r^2}{f} \quad (28)$$

using the $n(r)$ found above. The physical path length PPL_0 from the output surface of the lens to the isophase surface is

$$PPL_0(r) = \frac{OPL_0}{n_0} = \frac{1}{2} \frac{r^2}{f} \quad (29)$$

We thus see that the isophase surface has the shape of a parabola with its vertex at the center of the output side of the lens. The radius of curvature of this parabola at its vertex is f (not to be confused with the focal length of a parabolic mirror of the same shape, which is actually $f/2$). This matching to the desired spherical isophase surface's radius of curvature explains why the parabolic index profile is sufficient in the paraxial/low-power approximation.